nanomaterials

MDPI

Article

Sustainable Green Synthesis of Fe_3O_4 Nanocatalysts for Efficient Oxygen Evolution Reaction

Erico R. Carmona [1,2], Anandhakumar Sukeri [3,*], Ronald Nelson [4], Cynthia Rojo [1,2], Arnoldo Vizcarra [5], Aliro Villacorta [1,2], Felipe Carevic [1,2], Ricard Marcos [6], Bernardo Arriaza [5], Nelson Lara [5], Tamara Martinez [4] and Lucas Patricio Hernández-Saravia [1,2,*]

1 Laboratorio de Bionanomateriales, Facultad de Recursos Naturales Renovables, Universidad Arturo Prat, Campus Huayquique, Iquique 1100000, Chile; fcarevic@unap.cl (F.C.)
2 Núcleo de Investigación Aplicada e Innovación en Ciencias Biológicas, Facultad de Recursos Naturales Renovables, Universidad Arturo Prat, Av. Arturo Prat s/n, Campus Huayquique, Iquique 1100000, Chile
3 Department of Chemistry, Faculty of Engineering and Technology, SRM Institute of Science and Technology, Kattankulathur 630 203, Tamil Nadu, India
4 Departamento de Química, Facultad de Ciencias, Universidad Católica del Norte, Avda. Angamos 0610, Antofagasta 1270709, Chile; rnelson@ucn.cl (R.N.)
5 Campus Velasquez, Universidad de Tarapacá, Arica 1000007, Chile
6 Grup de Mutagenesi, Departament de Genética i de Microbiologia, Facultat de Biociencies, Universitat Autònoma de Barcelona, 08193 Barcelona, Spain; ricard.marcos@uab.cat
* Correspondence: anandhas2@srmist.edu.in (A.S.); luhernande@unap.cl (L.P.H.-S.)

Abstract

This work focuses on the sustainable green synthesis of magnetic iron oxide nanoparticles (Fe_3O_4NPs) using bioreductants derived from orange peel extracts for application in the efficient oxygen evolution reactions (OER). The synthesized catalysts were characterized using X-ray diffraction analysis, field emission scanning electron microscopy (FESEM), energy dispersive X-ray analysis (EDS), transmission electron microscopy (TEM), Fourier transform infrared spectroscopy (FTIR), and UV–visible spectroscopy. The Fe_3O_4NPs exhibit a well-defined spherical morphology with a larger Brunauer–Emmett–Teller surface area and a significant electrochemically active surface area. The green synthesis using orange peel extracts leads to an excellent electrocatalytic activity of the apparent spherical Fe_3O_4NPs (diameter of 9.62 $\pm$ 0.07 nm), which is explored for OER in an alkaline medium (1.0 M KOH) using linear-sweep and cyclic voltammetry techniques. These nanoparticles achieved a benchmark current density of 10 mA cm^{-2} at a low overpotential of 0.3 V versus RHE, along with notable durability and stability. The outstanding OER electrocatalytic activity is attributed to their unique morphology, which offers large surface area and an ideal porous structure that enhances the adsorption and activation of reactive species. Furthermore, structural defects within the nanoparticles facilitate efficient electron transfer and migration of these species, further accelerating the OER process.

Keywords: green synthesis; Fe_3O_4 nanoparticles; Electrocatalysis; oxygen evolution reaction; Sustainability

Academic Editors: Stefano Trocino and Fausta Giacobello

Received: 18 June 2025
Revised: 12 July 2025
Accepted: 15 July 2025
Published: 27 August 2025

Citation: Carmona, E.R.; Sukeri, A.; Nelson, R.; Rojo, C.; Vizcarra, A.; Villacorta, A.; Carevic, F.; Marcos, R.; Arriaza, B.; Lara, N.; et al. Sustainable Green Synthesis of Fe_3O_4 Nanocatalysts for Efficient Oxygen Evolution Reaction. *Nanomaterials* **2025**, *15*, 1317. https://doi.org/10.3390/nano15171317

1. Introduction

In recent years, the world's population has increased exponentially, resulting in a significant rise in CO_2 emissions from fossil fuels [1]. This has had a significant impact on the environment, which is why there is global interest in developing renewable and sustainable fuels that emit minimal to zero greenhouse gases [2]. The electrochemical

splitting [3] of water is one of the most attractive methods for hydrogen and oxygen generation with zero-carbon emission. In this process, the hydrogen evolution reaction (HER) and oxygen reduction reaction (ORR) [4] occur in the cathode [5–8], while the oxygen evolution reaction (OER) takes place in the anode. However, the sluggish OER kinetics at the anode affect the overall potential of the water splitting. In other words, a high potential must be applied for the transfer of the four electrons of the reaction, as described by the half-reaction $2H_2O \rightarrow O_2 + 4H^+ + 4e^-$ ($E^\circ = 1.23$ V at pH = 0), making this process highly inefficient [9]. Therefore, the development of new materials with high electrocatalytic efficiency and stability is essential for CO_2-free sustainable fuel production.

The current anode used in OER relies on electrocatalysts made from noble metals such as Pt, or noble metal oxides such as RuO_2 and IrO_2 [10–12]. These materials are not only scarce and expensive, but their electrocatalytic performance is often limited to high current densities. As a result, scaling up this process for industrial applications is not feasible [13,14]. To overcome these challenges, it is crucial to develop highly stable, efficient, cost-effective catalysts that possess superior catalytic activity [15]. Recently, several groups have investigated different nanomaterials for OER [16]; however, transition metals are a popular choice due to their low cost and abundance, such as Co_3O_4NPs [17], CoEDA [18], Mn_3O_4 [19], Ni/NiSPx/NF [20], WCx/CC [21], NiFe-LDH [22], Ni-MOF/$NiFe_2O_4$ [23], 3NiFe-1N-GA-800 [24], and FeCoNiCuMo-O [25], among others. Among these, magnetite nanoparticles (Fe_3O_4 NPs) have garnered significant interest for OER [26–30] due to their excellent magnetic and catalytic properties, as well as their low cost and abundance [31,32].

Furthermore, it is essential to evaluate the different synthesis methods for preparing Fe_3O_4 NPs. Several approaches are available, including solvothermal [33,34], ultrasonic/co-precipitation [35], co-precipitation [36], hydrothermal [37], sol–gel [38], microemulsion [39], and electrospinning [40]. However, despite the wide range of available methods for synthesizing Fe_3O_4NPs, many of them involve high costs, complex procedures, and the generation of toxic waste. In contrast, sustainable and ecological methods offer an attractive alternative, reducing environmental impact and promoting more environmentally friendly practices [41,42]. Nanomaterials with diverse sizes and shapes have been prepared through green synthesis [43,44], using different plant-based extracts as bioreductants. These include organic waste [45], *P. benghalensis* leaves [46], banana peels (*Musa paradisiaca*) [47], black tea leaves (*Camellia sinensis*) [48], *Citrus medica* Linn. (Idilimbu) juice [49], lemon peels [50], mango extract [51], and orange peels [52]. Also, it is worth noting that the global production of oranges is approximately 52 million tons, which results in a significant amount of organic waste in the form of orange peels. Additionally, iron is abundantly present in oranges. In this study, we propose an environmentally friendly, simple, and sustainable approach for producing Fe_3O_4 NPs using orange peel residues as bio-reducing agents for efficient OER.

2. Results

2.1. Materials Characterization Using X-Ray Diffraction and Microscopy Analysis

Figure 1 shows the XRD pattern of magnetite Fe_3O_4. The obtained 2θ values are 30.2° (200), 35.6° (311), 43.4° (400), 57.3° (511), and 62.8° (440), in agreement with previous reports, confirming the cubic spinel structure of magnetite Fe_3O_4. These peaks are consistent with studies carried out by Selvaraj et al. [53] and Elizondo et al. [54], indicating that the peaks at 2θ values of 43.4° and 57.3° correspond to (400) and (511) crystalline planes of Fe_3O_4 with rhombohedral structures. In addition, such results are also consistent with the reference JCPDS (19-0629) pattern of magnetite Fe_3O_4 (see Figure 1A,B).

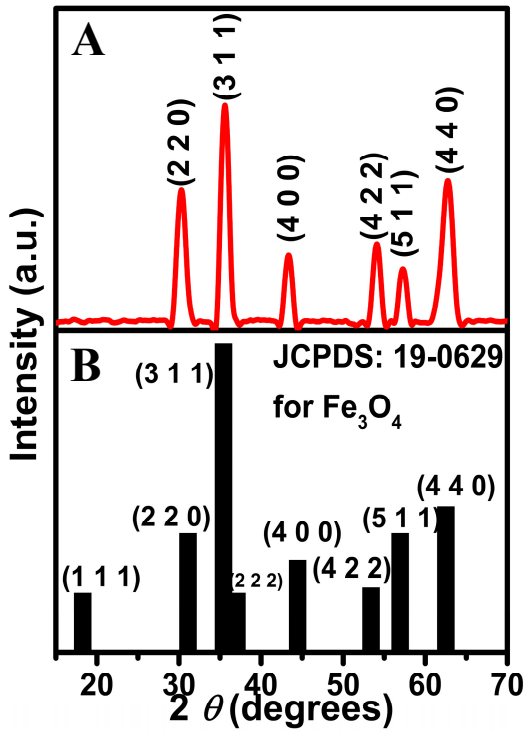

Figure 1. (**A**) XRD pattern of the synthesized Fe_3O_4 NPs; (**B**) corresponding JCPDS file: 19-0629.

The surface morphology of the Fe_3O_4 NPs was analyzed by SEM and TEM analysis (Figure 2A,B). The images reveal a predominantly spherical morphology, and the particle size distribution histogram (Inset, Figure 2B) shows particle sizes between 7.8 nm and 11.7 nm, with an average size of 9.62 ± 0.07 nm. The nanoparticle size obtained in this study is smaller than those reported for Fe_3O_4 NPs synthesized by other methods (Table S1).

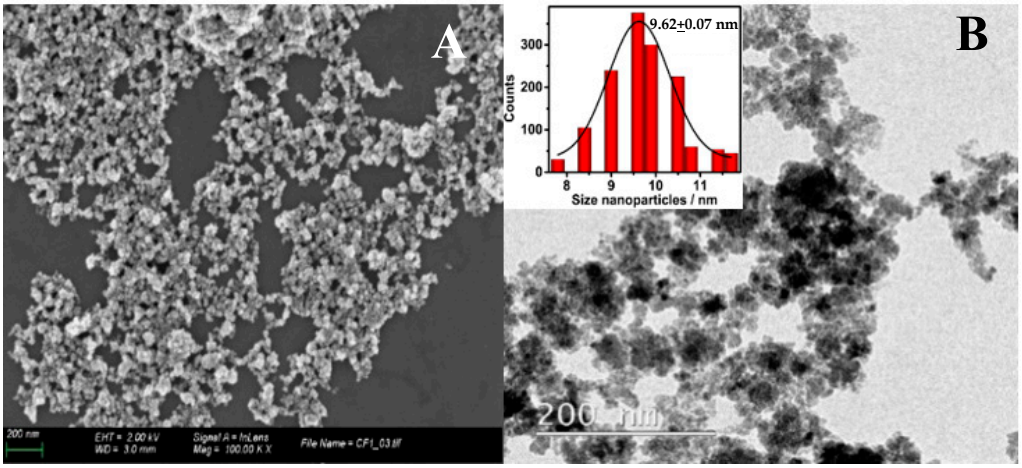

Figure 2. (**A**) SEM and (**B**) TEM image of Fe_3O_4 NPs (inset: size distribution histogram).

Additionally, the elemental composition of the Fe_3O_4 NPs was analyzed using energy-dispersive X-ray (EDX) analysis along with elemental mapping (Figure 3). The results show strong signals in the oxygen and iron regions, confirming the presence of Fe_3O_4 NPs. Figure S1 corroborated the presence of Fe and O, indicating the expected chemical composition of the Fe_3O_4NPs; a signal for aluminum was also detected, attributed to the sample holder. Moreover, signals corresponding to carbon (C), oxygen (O), and sulfur (S) were observed,

which is likely due to the presence of polyphenols from the organic extracts capping the Fe_3O_4 NPs, thereby contributing to their stabilization [55].

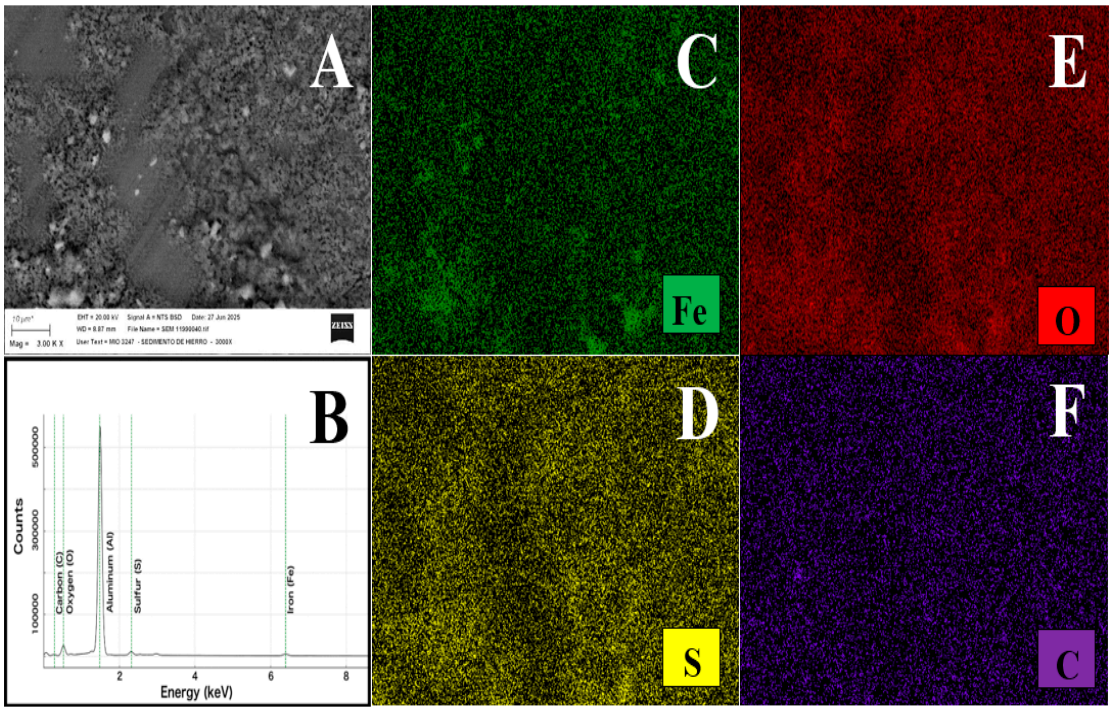

Figure 3. The SEM image of Fe_3O_4 NPs (**A**), EDX analysis and its elemental mapping for Fe_3O_4 NPs (**B**), and the presence of Fe (**C**), S (**D**), O (**E**), and C (**F**) atoms in the Fe_3O_4 NPs.

2.2. UV–Visible and FT-IR Analysis

The results of the UV–visible characterization of the synthesized Fe_3O_4 NPs are shown in Figure 4A. Absorption peaks observed at 240, 270, and 340 nm indicate the presence of polyphenols from the orange peel extract. These results are consistent with previous reports by Zayed et al. [56], who observed similar peaks related to the polyphenol content in plant leaf infusions. In comparison with the Fe^{2+}/Fe^{3+} precursor salts, the absorbance peak at 350 nm (green line in Figure 4A) suggests the reduction in Fe ions and supports the formation of Fe_3O_4 NPs [52,57,58].

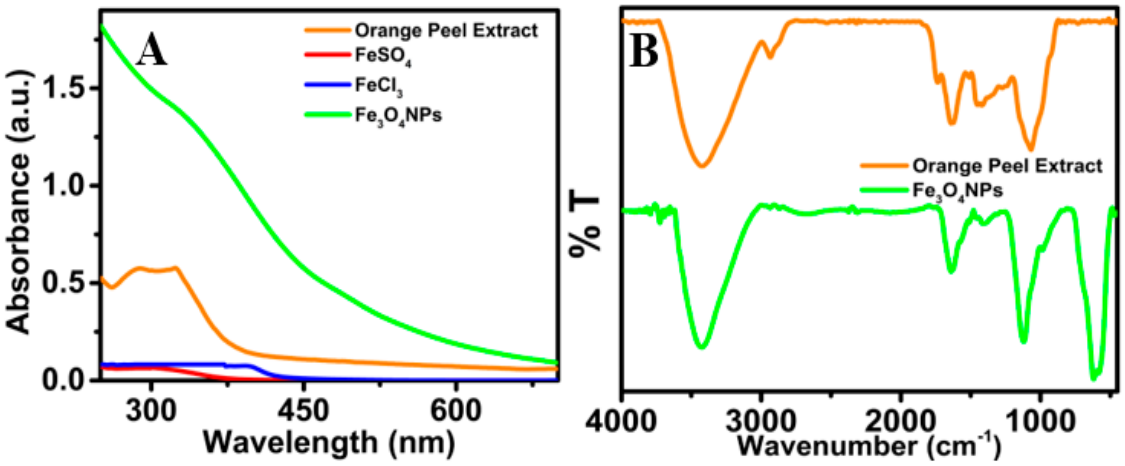

Figure 4. (**A**) UV–vis absorption spectra of Fe_3O_4 NPs synthesized with 0.5% of orange peel extract and Fe salts (**B**); FTIR spectra of Fe_3O_4 NPs synthesized using orange peel extract (green line) and orange peel extract (orange line).

Figure 4B presents the FTIR spectra of Fe_3O_4 NPs and the orange peel extract. The main absorption bands observed at 547, 1033, 1635, and 3540 cm^{-1} (see Table 1) are attributed to the Fe-O, S=O, C=C, and –OH, respectively [59,60]. Notably, the Fe-O characteristic peak (547 cm^{-1}) appeared only in the Fe_3O_4 NPs spectrum.

Table 1. FTIR analysis of Fe_3O_4NPs and orange peel extract containing possible functional groups.

Fe_3O_4 NPs Wavenumber (cm^{-1})	Functional Groups	Orange Peel Extract Wavenumber (cm^{-1})	Functional Groups
547	Strong Fe–O	547	-
1033	Medium S=O	1033	Medium S=O
1635	Medium C=C	1635	Medium C=C
3540	Board O–H	3540	Board O–H

2.3. Prepared Fe_3O_4NPs by BET Analysis

Table 2 shows the measured specific surface area (SSA) of the Fe_3O_4 nanoparticles (NPs), which was found to be 80.37 m^2 g^{-1}. The total pore volume (PV) of Fe_3O_4NPs was 0.274 cm^3 g^{-1}, and the average PS value recorded was 4.66 nm. The high pore volume indicates a high degree of porosity, suggesting a large number of sites, which favors the electrocatalytic performance of the Fe_3O_4NPs. The BET surface area of Fe_3O_4NPs was calculated to be 80.37 m^2 g^{-1}, considerably higher than the values reported by various chemical and green synthesis methods (Table S2).

Table 2. The tabulated values of BET surface area (m^2 g^{-1}), pore volume (cm^3 g^{-1}), and pore size (nm) of Fe_3O_4NPs.

Nanoparticles	BET Surface Area (m^2 g^{-1})	Pore Volume (cm^3 g^{-1})	Pore Size (nm)
Fe_3O_4NPs	80.37	0.274	4.66

2.4. Electrochemical Characterization of Fe_3O_4NPs

The larger accessible surface area of Fe_3O_4NPs indicates their superior electron-transferring capabilities during redox reactions. To further investigate this, the electrochemical active surface area (ECSA) of the Fe_3O_4NPs was calculated using the Randles–Sevcik Equation (1) [61].

$$i_p = \left(2.69 \times 10^5\right) n^{3/2} D^{1/2} \nu^{1/2} AC \quad (1)$$

This equation relates the peak current (Ipa) to the number of electrons transferred (n = 1), the diffusion coefficient (D) of the $[Fe(CN)_6]^{3-/4-}$ redox probe (7.60 × 10^{-6} cm^2 s^{-1}), the scan rate (ν), the active surface area (A), and the concentration (C of 1 × 10^{-6} mol cm^{-3}). The ECSA of Fe_3O_4NPs was determined by measuring the redox peak current across scan rates ranging from 0.005 to 0.150 V s^{-1} (as shown in Figure 5). An increase in the scan rate led to a more pronounced redox peak current response with changes in redox peak potential, which is attributed to rapid electron transport facilitated by the Fe_3O_4NPs. Furthermore, a strong linear relationship was observed between the redox peak current and the square root of the scan rate (with correlation coefficients of 0.9988 for I_{pa} and 0.9971 for I_{pc}), consistent with a diffusion-controlled electrode process.

From the slope of this linear plot, the ECSA of the Fe_3O_4NPs was calculated to be approximately 0.198 cm^2. This value represents a significant enhancement, being 2.7 times greater than the ECSA of a bare glassy carbon electrode (GCE), which was measured at 0.07065 cm^2. These findings conclusively demonstrate that Fe_3O_4NPs possess both a high surface area and efficient electron transfer properties, suggesting their promising application as an effective electrode modification in electrochemical detection research.

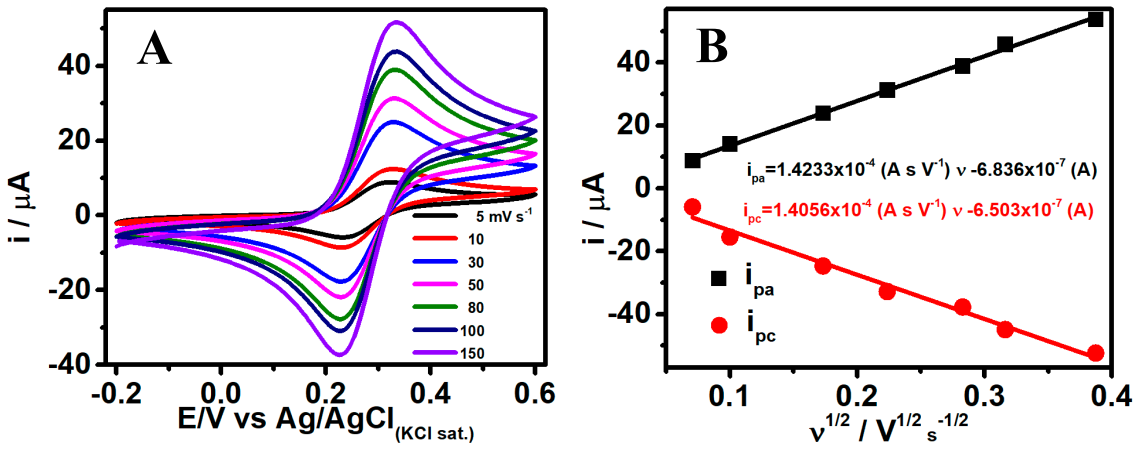

Figure 5. (**A**) CVs of Fe_3O_4NPs at different scan rates (0.005–0.150 V s^{-1}) and (**B**) corresponding linear plot of the square root of scan rate vs. i. The $[Fe(CN)_6]^{3-/4-}$ system was used for electrochemical characterization studies.

2.5. Electrochemical Studies for the Oxygen Evolution Reaction

The electrochemical performance of GCE and Fe_3O_4NPs/GCE was evaluated towards oxygen evolution reaction (OER) by recording the linear sweep voltammogram (LSV) in a 1.0 M KOH solution (pH = 14) at the scan rate of 2 mV s^{-1} (Figure 6A). The Fe_3O_4 NPs/GCE exhibited significantly enhanced electrocatalytic activity compared to the bare GCE, as evidenced by a lower onset potential and a marked increase in current density. Moreover, the benchmark current density of 10 mA cm^{-2} was achieved at a very low overpotential of 0.3 V vs. RHE, which is 0.28 V less overpotential than GCE (0.58 V). This improved performance can be attributed to the increased surface area and roughness of the Fe_3O_4 NPs/GCE, resulting from the small particle size, enlarging the number of active sites and enhancing the electrocatalytic activity of OER. In addition, the Tafel slope was calculated from the Tafel plot (η vs. Log j) using the LSV data obtained from Figure 6B, and the value was found to be 95.8 mV dec^{-1} for Fe_3O_4 NPs/GCE. Furthermore, the OER performance of the nanocatalyst was compared with other Fe-based catalysts reported in the literature (Table 3), showing that the present system exhibits notably improved performance relative to previously reported values. The stability of OER at the benchmark current density of 10 mA cm^{-2} was also tested using LSV polarization curves (Figure 6C) and amperometry (Figure 6D). LSV recorded at the 1st, 1000th, and 2000th cycle showed negligible variation in performance, indicating stable electrocatalytic activity over prolonged cycling. In addition, there is no significant change in the current response of 10 mA cm^{-2} over 48 h in the amperometry measurement (at an applied overpotential of 0.3 V). These results demonstrate the efficient durability and stability of Fe_3O_4NPs/GCE catalyst for OER. The OER mechanism is complex and can proceed via different pathways, but a common one is the oxide path, which based on the results obtained from Fe_3O_4NPs and what was reported by Soni A. et al. [62] suggests that the OER follows the following mechanism:

$$M + OH^- \rightarrow M - OH + \bar{e}$$

$$M - OH + OH^- \rightarrow M - O + H_2O + \bar{e}$$

$$M - O \rightarrow 2M + O_2$$

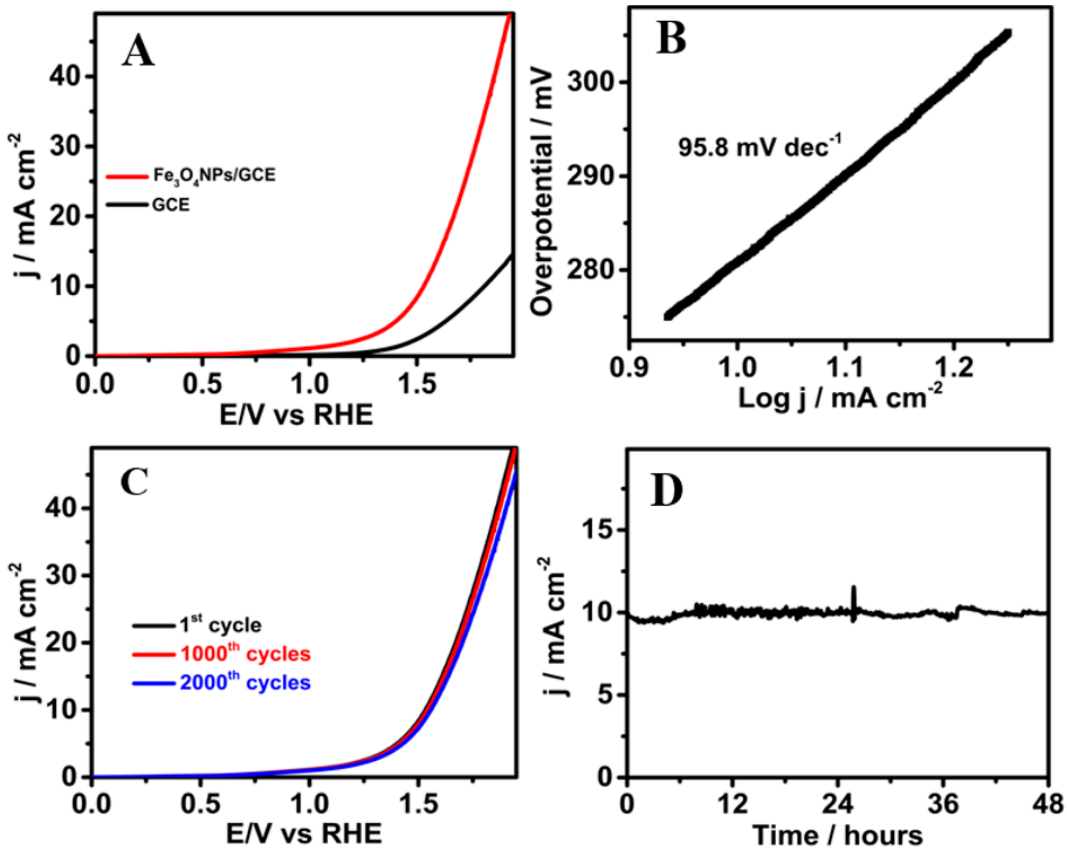

Figure 6. (**A**) LSV polarization curves recorded in 1.0 M KOH solution with GCE (black) and Fe_3O_4 NPs/GCE (red) electrodes at the scan rate of 2 mV s^{-1}. (**B**) Tafel plot, (**C**) durability in 1.0 M KOH solution after 1000 and 2000 cycles, and (**D**) amperometric curves at an applied overpotential of 0.3 V for Fe_3O_4 NPs/GCE.

Table 3. Comparison of Fe-based nanocatalysts for OER performances.

Materials	Electrolytes	Overpotential (V) (at 10 mA cm^{-2})	Ref.
$(NiFe)S_2$	1.0 M KOH	0.32	[63]
porous Ni–FeO	1.0 M KOH	0.33	[64]
NiFe@NC	1.0 M KOH	0.58	[65]
$FePO_4$/NF	1.0 M KOH	0.31	[66]
Fe-doped NiO_x	1.0 M KOH	0.31	[67]
$Ni_{0.62}Fe_{0.38}P$	1.0 M KOH	0.31	[68]
$Ni_{1.5}Fe_{0.5}P$/CF	1.0 M KOH	0.36	[69]
S-$NiFe_2O_4$/NF	1.0 M KOH	0.42	[70]
NiFeOCPc@rGO-K	1.0 M KOH	0.37	[9]
$Fe_{0.22}Ni_{0.78}(OH)_2$	1.0 M KOH	0.32	[71]
NiO_x–NiO_x/FeO_x	1.0 M KOH	0.32	[72]
Fe_3O_4/graphene	0.1 M KOH	-	[73]
FeCoV-NiMOF	0.1 M KOH	0.238	[74]
Fe_3O_4-600	1.0 M NaOH	0.33	[28]
Fe_3O_4NPs	**1.0 M KOH**	**0.30**	**This work**

3. Materials and Methods

3.1. Chemicals

Iron (II) sulfate ($FeSO_4$), iron (III) chloride ($FeCl_3$), Nafion (5 wt%), ethanol (C_2H_5OH), and potassium hydroxide (KOH) were used as received from Sigma-Aldrich and Merck, respectively. High-purity argon and oxygen gases were purchased from local suppliers. Unless otherwise stated, all the aqueous solutions were prepared using Milli-Q water with 18.0 MΩ cm resistivity.

3.2. Instruments

Electrochemical measurements were carried out using an Autolab Origaflex OGF 01A potentiostat with OrigaMaster 5 software. A glassy carbon electrode (GCE) and/or a Fe_3O_4 nanoparticles-modified glassy carbon electrode (Fe_3O_4 NPs/GCE) was used as working electrode, while an Ag/AgCl electrode (saturated KCl) and a platinum wire served as the reference and counter electrodes, respectively. All potentials in this work are reported vs. the reversible hydrogen electrode (RHE), where E (vs. RHE) = E (vs. Ag/AgCl) + 0.0592 × pH + 0.197 V at 25 °C. The formation of Fe_3O_4 nanoparticles was monitored with a UV–visible spectrophotometer (Spectroquant® Prove 300, Merck, Germany), operating with a 1 nm interval and integration time of 1 s, over a wavelength a range of 200–800 nm. FTIR analyses were conducted using an FT/IR 4X spectrometer (Jasco, USA). The samples were analyzed using an ATR accessory to examine the surface functional groups of the reduced Fe_3O_4NPs. The FTIR spectra were collected at a spatial resolution of 4 cm^{-1} in the transmission mode, between 4000 and 400 cm^{-1}. The XRD analysis of the samples was carried out in an X-ray diffractometer (Bruker, Model D8 Advance, USA) using a Vertical Bragg–Brentano goniometer, a solid-state detector (Centelleo Model), with Cu Ka radiation operating at 40 kV and 30 mA. The topography of the synthesized Fe_3O_4 NPs was examined using a JEM 1400 transmission electron microscope (JEOL Ltd., Tokyo, Japan). For TEM analysis, Fe_3O_4 NPs were re-suspended in water at a concentration of 0.1 mg mL^{-1}, sonicated for 30 min, and 100 µL of the suspension was mixed with silver epoxy adhesive and deposited on a silica film. The sample was then dried in an oven at 60 °C until complete evaporation of water, prior to TEM imaging. Surface characterization of Fe_3O_4 NPs was conducted using an SEM instrument (Zeiss Merlin, Oberkochen, Germany). The processing of SEM micrographs was interpreted using ImageJ win32 software.

3.3. Preparation of Orange Peel Extract

The orange peels were thoroughly washed with deionized water to remove any surface impurities. They were then dried in an oven at 60 °C for 36 h. Once dried, the peels were crushed with a mini blender until a fine powder of 5 µm ± 0.5 µm was obtained. Subsequently, the orange peel extract was prepared by dispersing 40 g of powdered peel per liter of deionized water, followed by stirring at 1000 rpm at 80 °C for 2 h. The resulting extract was then filtered and stored at −4 °C.

3.4. Green Synthesis of Fe_3O_4 Nanoparticles

The green synthesis of Fe_3O_4 NPs was carried out by mixing $FeSO_4$ and $FeCl_3$ salts in a 2:1 ratio of 10 mM. Under constant stirring, the orange peel extract was added dropwise to the Fe salts solution, and the pH was adjusted to 10. The solution was stirred for 30 min at 300 rpm. Once this process was finished, the final solution was allowed to decant to remove the supernatant. The resulting Fe_3O_4 NPs were collected, washed with ethanol, and dried in an oven at 60 °C for 24 h, as shown in Scheme 1.

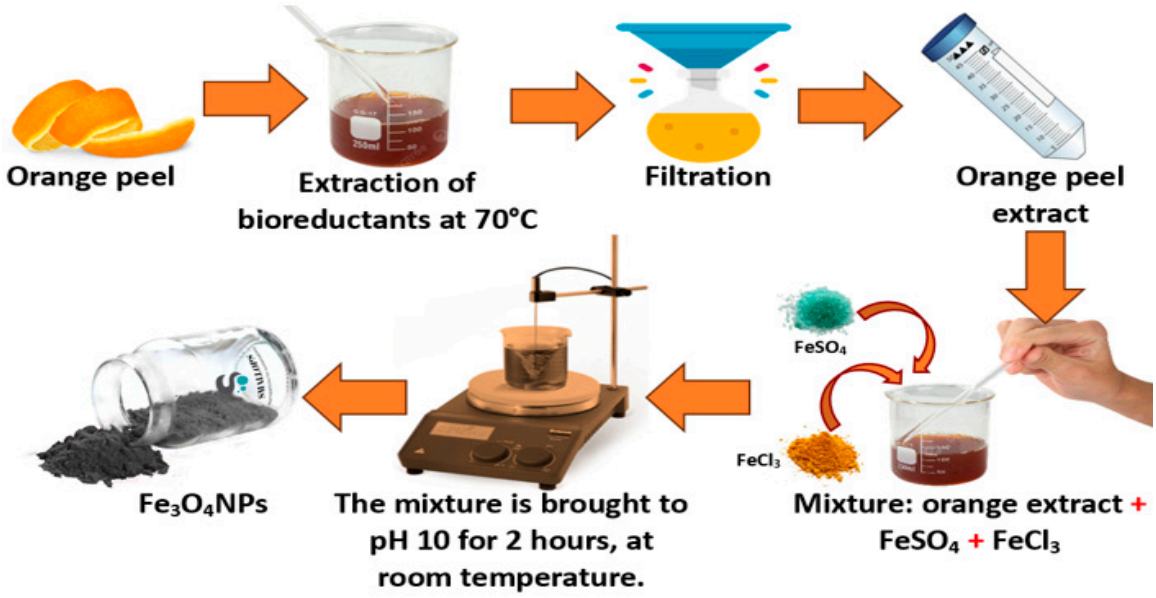

Scheme 1. Fabrication procedure of Fe_3O_4 NPs using orange peel extracts by eco-friendly green synthesis method.

3.5. Preparation of Fe_3O_4 NPs Modified Glassy Carbon Electrode (GCE)

The GCE was carefully polished using a polishing cloth and 0.05 µm alumina powder, followed by sonication for 15 min in an aqueous solution. Fe_3O_4 NPs (2 mg mL^{-1}) were dispersed in water, and Nafion (0.1%) solution was added. The mixture was sonicated for 10 min to obtain a homogeneous suspension. Subsequently, 10 µL of the suspension was drop-cast on the surface of the GCE and allowed to dry at room temperature.

4. Conclusions

This work successfully demonstrates the sustainable green synthesis of Fe_3O_4 nanocatalysts using orange peel extracts, which exhibit excellent electrocatalytic activity for the OER. These nanoparticles, with an average diameter of 9.62 ± 0.07 nm, achieve a benchmark current density of 10 mA cm^{-2} at a low overpotential of 0.3 V versus RHE, along with remarkable durability and stability. This high performance is attributed to their unique morphology, large surface area, and porous structure, which facilitate efficient adsorption, activation of reactive species, and electron transfer. These findings present a promising pathway for developing novel, cost-effective, and efficient Fe-based nanocatalysts for applications in energy conversion, sustainable chemistry, and electrochemistry.

Supplementary Materials: The following supporting information can be downloaded at https://www.mdpi.com/article/10.3390/nano15171317/s1, Table S1. Size and shape comparison of the synthesized Fe_3O_4 nanocatalyst with the literature. Figure S1. SEM image of elemental mapping distribution Fe_3O_4NPs for Fe, O, S and C respectively.

Author Contributions: E.R.C.: methodology, formal analysis, investigation, writing—original draft preparation, A.S.: conceptualization, writing—original draft preparation, writing—review and editing, R.N.: investigation, C.R.: methodology, formal analysis, A.V. (Arnoldo Vizcarra): formal analysis, A.V. (Aliro Villacorta): formal analysis, investigation, F.C.: formal analysis, investigation R.M.: methodology, resources, B.A.: resources, writing—original draft preparation, N.L.: methodology, writing—original draft preparation, T.M.: formal analysis, and L.P.H.-S.: conceptualization, writing—original draft preparation, writing—review and editing, supervision. All authors have read and agreed to the published version of the manuscript.

Funding: FONDEF supported this work with financial support (Grant ID 21I10130). This research was funded by Vicerrectoria de investigación Universidad Arturo Prat. N.L. thanks UTA Mayor 4773-25 for funding.

Data Availability Statement: Data are contained within the article and Supplementary Materials.

Conflicts of Interest: No potential conflicts of interest were reported by the authors.

References

1. Sharma, S.; Sharma, V.; Chatterjee, S. Contribution of Plastic and Microplastic to Global Climate Change and Their Conjoining Impacts on the Environment—A Review. *Sci. Total Environ.* **2023**, *875*, 162627. [CrossRef] [PubMed]
2. Aravindan, M.; Kumar, V.M.; Hariharan, V.S.; Narahari, T.; Kumar, P.A.; Madhesh, K.; Kumar, G.P.; Prabakaran, R. Fuelling the Future: A Review of Non-Renewable Hydrogen Production and Storage Techniques. *Renew. Sustain. Energy Rev.* **2023**, *188*, 113791. [CrossRef]
3. Jamadar, A.S.; Sutar, R.; Patil, S.; Khandekar, R.; Yadav, J.B. Progress in Metal Oxide-Based Electrocatalysts for Sustainable Water Splitting. *Mater. Rep. Energy* **2024**, *4*, 100283. [CrossRef]
4. Zheng, Y.; Zhao, Y.; Luo, W.; Zhang, Y.; Wang, Y.; Wu, Y. Rational Design Strategies for Covalent Organic Frameworks Toward Efficient Electrocatalytic Hydrogen Peroxide Production. *Catalysts* **2025**, *15*, 500. [CrossRef]
5. Quezada, V.; Martinez, T.; Nelson, R.; Pérez-Fehrmann, M.; Zaragoza, G.; Vizcarra, A.; Kesternich, V.; Hernández-Saravia, L.P. A Novel Platform of Using Copper (II) Complex with Triazole-Carboxilated Modified as Bidentated Ligand SPCE for the Detection of Hydrogen Peroxide in Milk. *J. Electroanal. Chem.* **2020**, *879*, 114763. [CrossRef]
6. Silva, T.R.; Raimundo, R.A.; Silva, V.D.; Santos, J.R.D.; Araújo, A.J.M.; Oliveira, J.F.G.d.A.; de Lima, L.C.; da Silva, F.F.; Ferreira, L.d.S.; Macedo, D.A. Green Synthesis of $CuCo_2O_4$–CuO Composite Nanoparticles Grown on Nickel Foam for High-Performance Oxygen Evolution Reaction. *Int. J. Hydrogen Energy* **2023**, *48*, 17160–17176. [CrossRef]
7. Hernández-Saravia, L.P.; Sukeri, A.; Bertotti, M. Fabrication of Nanoporous Gold-Islands via Hydrogen Bubble Template: An Efficient Electrocatalyst for Oxygen Reduction and Hydrogen Evolution Reactions. *Int. J. Hydrogen Energy* **2019**, *44*, 15001–15008. [CrossRef]
8. Aralekallu, S.; Hadimane, S.; Shantharaja; Nemakal, M.; Koodlur Sannegowda, L. Organic Hybrid of Cobalt Phthalocyanine Embedded Graphene as an Efficient Catalyst for Oxygen Reduction Reaction. *Fuel* **2024**, *361*, 130736. [CrossRef]
9. Gonçalves, J.M.; Matias, T.A.; Saravia, L.P.H.; Nakamura, M.; Bernardes, J.S.; Bertotti, M.; Araki, K. Synergic Effects Enhance the Catalytic Properties of Alpha-$Ni(OH)_2$-FeOCPc@rGO Composite for Oxygen Evolution Reaction. *Electrochim. Acta* **2018**, *267*, 161–169. [CrossRef]
10. Lee, Y.; Suntivich, J.; May, K.J.; Perry, E.E.; Shao-Horn, Y. Synthesis and Activities of Rutile IrO_2 and RuO_2 Nanoparticles for Oxygen Evolution in Acid and Alkaline Solutions. *J. Phys. Chem. Lett.* **2012**, *3*, 399–404. [CrossRef] [PubMed]
11. Xu, X.; Huang, Z.; Zhao, C.; Ding, X.; Liu, X.; Wang, D.; Hui, Z.; Jia, R.; Liu, Y. Interface Engineering of Copper-Cobalt Based Heterostructure as Bifunctional Electrocatalysts for Overall Water Splitting. *Ceram. Int.* **2020**, *46*, 13125–13132. [CrossRef]
12. Bolar, S.; Shit, S.; Chandra Murmu, N.; Kuila, T. Progress in Theoretical and Experimental Investigation on Seawater Electrolysis: Opportunities and Challenges. *Sustain. Energy Fuels* **2021**, *5*, 5915–5945. [CrossRef]
13. Huang, C.-J.; Xu, H.-M.; Shuai, T.-Y.; Zhan, Q.-N.; Zhang, Z.-J.; Li, G.-R. A Review of Modulation Strategies for Improving Catalytic Performance of Transition Metal Phosphides for Oxygen Evolution Reaction. *Appl. Catal. B Environ.* **2023**, *325*, 122313. [CrossRef]
14. Jung, H.; Karmakar, A.; Adhikari, A.; Patel, R.; Kundu, S. Graphene-Based Materials as Electrocatalysts for the Oxygen Evolution Reaction: A Review. *Sustain. Energy Fuels* **2022**, *6*, 640–663. [CrossRef]
15. Li, H.; Xu, S.; Yan, H.; Yang, L.; Xu, S. Cobalt Phosphide Composite Encapsulated within N,P-Doped Carbon Nanotubes for Synergistic Oxygen Evolution. *Small* **2018**, *14*, e1800367. [CrossRef] [PubMed]
16. Sun, H.; Xu, X.; Chen, G.; Zhou, Y.; Lin, H.; Chen, C.; Ran, R.; Zhou, W.; Shao, Z. Smart Control of Composition for Double Perovskite Electrocatalysts toward Enhanced Oxygen Evolution Reaction. *ChemSusChem* **2019**, *12*, 5111–5116. [CrossRef] [PubMed]
17. Paul, B.; Bhanja, P.; Sharma, S.; Yamauchi, Y.; Alothman, Z.A.; Wang, Z.-L.; Bal, R.; Bhaumik, A. Morphologically Controlled Cobalt Oxide Nanoparticles for Efficient Oxygen Evolution Reaction. *J. Colloid Interface Sci.* **2021**, *582*, 322–332. [CrossRef] [PubMed]
18. Bhanja, P.; Mohanty, B.; Paul, B.; Bhaumik, A.; Jena, B.K.; Basu, S. Novel Microporous Organic-Inorganic Hybrid Metal Phosphonates as Electrocatalysts towards Water Oxidation Reaction. *Electrochim. Acta* **2022**, *416*, 140277. [CrossRef]
19. Chowde Gowda, C.; Mathur, A.; Parui, A.; Kumbhakar, P.; Pandey, P.; Sharma, S.; Chandra, A.; Singh, A.K.; Halder, A.; Tiwary, C.S. Understanding the Electrocatalysis OER and ORR Activity of Ultrathin Spinel Mn_3O_4. *J. Ind. Eng. Chem.* **2022**, *113*, 153–160. [CrossRef]

20. Yang, L.; Yang, T.; Wang, E.; Yu, X.; Wang, K.; Du, Z.; Cao, S.; Chou, K.-C.; Hou, X. Bifunctional Hierarchical NiCoP@FeNi LDH Nanosheet Array Electrocatalyst for Industrial-Scale High-Current-Density Water Splitting. *J. Mater. Sci. Technol.* **2023**, *159*, 33–40. [CrossRef]
21. Shen, P.; Guan, L.; Zhang, Z.; Zhao, J.; Yang, Y.; Wu, L.; Huang, Y.; Li, M.; Song, X. Fast Joule Heating Preparation and Performance Study of Carbon-Loaded Nano Tungsten-Based Electrocatalysts for Highly Efficient Oxygen Evolution Reaction. *ACS Appl. Energy Mater.* **2025**, *8*, 7095–7106. [CrossRef]
22. Wu, F.; Tian, F.; Li, M.; Geng, S.; Qiu, L.; He, L.; Li, L.; Chen, Z.; Yu, Y.; Yang, W.; et al. Engineering Lattice Oxygen Regeneration of NiFe Layered Double Hydroxide Enhances Oxygen Evolution Catalysis Durability. *Angew. Chem. Int. Ed.* **2025**, *64*, e202413250. [CrossRef] [PubMed]
23. Guo, X.-Y.; Yang, Z.-Q.; Zhao, J.; Liu, R. One-Pot Modulated Construction of Ni-MOF/$NiFe_2O_4$ Heterostructured Catalyst for Efficient Oxygen Evolution. *Rare Met.* **2024**, *43*, 6751–6757. [CrossRef]
24. Wu, X.; Gu, X.; Tai, J.; Tang, J.; Yuan, K.; Liu, L.; Zheng, Y.; Altaf, A.; Shen, X.; Cui, S. Facile Synthesis of the NiFe Bimetallic Alloy Wrapped on the Porous N-Doped Graphene Aerogel via Thermal Reduction and Electronic Structure Modulation for Boosting Oxygen Evolution Reaction. *J. Power Sources* **2025**, *633*, 236430. [CrossRef]
25. Liao, W.; Qing, F.; Liu, Q.; Wu, R.; Zhou, C.; Chen, L.; Chen, Y.; Li, X. Carbothermal Shock Synthesis of Lattice Oxygen-Mediated High-Entropy FeCoNiCuMo-O Electrocatalyst with a Fast Kinetic, High Efficiency, and Stable Oxygen Evolution Reaction. *Nano Lett.* **2025**, *25*, 1575–1583. [CrossRef] [PubMed]
26. Royer, L.; Guehl, J.; Zilbermann, M.; Dintzer, T.; Leuvrey, C.; Pichon, B.P.; Savinova, E.; Bonnefont, A. Influence of the Catalyst Layer Thickness on the Determination of the OER Activity of Fe_3O_4@$CoFe_2O_4$ Core-Shell Nanoparticles. *Electrochim. Acta* **2023**, *446*, 141981. [CrossRef]
27. Zhang, W.; Guan, H.; Hu, Y.; Wang, W.; Yang, X.; Kuang, C. Enhancing Catalytic Activity of Fe_3O_4 for Electrochemical Water Oxidation via the Coupling of OER-Inert Au. *Int. J. Hydrogen Energy* **2022**, *47*, 22731–22737. [CrossRef]
28. Wei, M.; Han, Y.; Liu, Y.; Su, B.; Yang, H.; Lei, Z. Green Preparation of Fe_3O_4 Coral-like Nanomaterials with Outstanding Magnetic and OER Properties. *J. Alloys Compd.* **2020**, *831*, 154702. [CrossRef]
29. Kashif Saleem, M.; Ahmad Niaz, N.; Fahmi Fawy, K.; Abdelmohsen, S.A.M.; Alanazi, M.M.; Hussain, F.; Naeem Ashiq, M.; Rasheed, U.; Abbas, Y.; Shuaib Khan, M. Electrocatalytic Behavior of Ni-Co-Fe_3O_4 Nanospheres for Efficient Oxygen Evolution Reaction. *J. Electroanal. Chem.* **2023**, *940*, 117503. [CrossRef]
30. Zhang, X.; Qiu, Y.; Li, Q.; Liu, F.; Cui, L.; Li, C.; Liu, J. Sandwich Structured Fe_3O_4/NiFe LDH/Fe_3O_4 as a Bifunctional Electrocatalyst with Superior Stability for Highly Sustained Overall Water Splitting. *J. Alloys Compd.* **2023**, *932*, 167612. [CrossRef]
31. Zhang, Z.; Zhou, D.; Liao, J.; Bao, X.; Luo, S. One-Pot Synthesis of Fe_3O_4/Fe/C by Microwave Sintering as an Efficient Bifunctional Electrocatalyst for Oxygen Reduction and Oxygen Evolution Reactions. *J. Alloys Compd.* **2019**, *786*, 134–138. [CrossRef]
32. Liu, G.; Yao, R.; Zhao, Y.; Wang, M.; Li, N.; Li, Y.; Bo, X.; Li, J.; Zhao, C. Encapsulation of Ni/Fe_3O_4 Heterostructures inside Onion-like N-Doped Carbon Nanorods Enables Synergistic Electrocatalysis for Water Oxidation. *Nanoscale* **2018**, *10*, 3997–4003. [CrossRef] [PubMed]
33. Fan, T.; Pan, D.; Zhang, H. Study on Formation Mechanism by Monitoring the Morphology and Structure Evolution of Nearly Monodispersed Fe_3O_4 Submicroparticles with Controlled Particle Sizes. *Ind. Eng. Chem. Res.* **2011**, *50*, 9009–9018. [CrossRef]
34. Hu, H.; Yang, L.; Lin, Z.; Xiang, X.; Jiang, X.; Hou, L. Preparation and Characterization of Novel Magnetic Fe_3O_4/Chitosan/$Al(OH)_3$ Beads and Its Adsorption for Fluoride. *Int. J. Biol. Macromol.* **2018**, *114*, 256–262. [CrossRef] [PubMed]
35. Wu, S.; Sun, A.; Zhai, F.; Wang, J.; Xu, W.; Zhang, Q.; Volinsky, A.A. Fe_3O_4 Magnetic Nanoparticles Synthesis from Tailings by Ultrasonic Chemical Co-Precipitation. *Mater. Lett.* **2011**, *65*, 1882–1884. [CrossRef]
36. Giri, S.K.; Das, N.N.; Pradhan, G.C. Synthesis and Characterization of Magnetite Nanoparticles Using Waste Iron Ore Tailings for Adsorptive Removal of Dyes from Aqueous Solution. *Colloids Surf. A Physicochem. Eng. Asp.* **2011**, *389*, 43–49. [CrossRef]
37. Cao, W.; Ma, Y.; Zhou, W.; Guo, L. One-Pot Hydrothermal Synthesis of RGO-Fe_3O_4 Hybrid Nanocomposite for Removal of Pb(II) via Magnetic Separation. *Chem. Res. Chin. Univ.* **2015**, *31*, 508–513. [CrossRef]
38. Li, J.; Wu, Y.; Yang, M.; Yuan, Y.; Yin, W.; Peng, Q.; Li, Y.; He, X. Electrospun Fe_2O_3 Nanotubes and Fe_3O_4 Nanofibers by Citric Acid Sol-gel Method. *J. Am. Ceram. Soc.* **2017**, *100*, 5460–5470. [CrossRef]
39. Nayeem, J.; Al-Bari, M.A.A.; Mahiuddin, M.; Rahman, M.A.; Mefford, O.T.; Ahmad, H.; Rahman, M.M. Silica Coating of Iron Oxide Magnetic Nanoparticles by Reverse Microemulsion Method and Their Functionalization with Cationic Polymer P(NIPAm-Co-AMPTMA) for Antibacterial Vancomycin Immobilization. *Colloids Surf. A Physicochem. Eng. Asp.* **2021**, *611*, 125857. [CrossRef]
40. Shi, S.; Xu, C.; Wang, X.; Xie, Y.; Wang, Y.; Dong, Q.; Zhu, L.; Zhang, G.; Xu, D. Electrospinning Fabrication of Flexible Fe_3O_4 Fibers by Sol-Gel Method with High Saturation Magnetization for Heavy Metal Adsorption. *Mater. Des.* **2020**, *186*, 108298. [CrossRef]

41. Saleh, T.A.; Fadillah, G. Green Synthesis Protocols, Toxicity, and Recent Progress in Nanomaterial-Based for Environmental Chemical Sensors Applications. *Trends Environ. Anal. Chem.* **2023**, *39*, e00204. [CrossRef]
42. Hernández-Saravia, L.P.; Carmona, E.R.; Villacorta, A.; Carevic, F.S.; Marcos, R. Sustainable Use of Mining and Electronic Waste for Nanomaterial Synthesis with Technological Applications: State of the Art and Future Directions. *Green Chem. Lett. Rev.* **2023**, *16*, 2260401. [CrossRef]
43. Brar, K.K.; Magdouli, S.; Othmani, A.; Ghanei, J.; Narisetty, V.; Sindhu, R.; Binod, P.; Pugazhendhi, A.; Awasthi, M.K.; Pandey, A. Green Route for Recycling of Low-Cost Waste Resources for the Biosynthesis of Nanoparticles (NPs) and Nanomaterials (NMs)-A Review. *Environ. Res.* **2022**, *207*, 112202. [CrossRef] [PubMed]
44. Goswami, A.D.; Trivedi, D.H.; Jadhav, N.L.; Pinjari, D.V. Sustainable and Green Synthesis of Carbon Nanomaterials: A Review. *J. Environ. Chem. Eng.* **2021**, *9*, 106118. [CrossRef]
45. Tripathi, N.; Pavelyev, V.; Islam, S.S. Synthesis of Carbon Nanotubes Using Green Plant Extract as Catalyst: Unconventional Concept and Its Realization. *Appl. Nanosci.* **2017**, *7*, 557–566. [CrossRef]
46. Paul, B.; Bhuyan, B.; Dhar Purkayastha, D.; Dey, M.; Dhar, S.S. Green Synthesis of Gold Nanoparticles Using Pogestemon Benghalensis (B) O. Ktz. Leaf Extract and Studies of Their Photocatalytic Activity in Degradation of Methylene Blue. *Mater. Lett.* **2015**, *148*, 37–40. [CrossRef]
47. Ibrahim, H.M.M. Green Synthesis and Characterization of Silver Nanoparticles Using Banana Peel Extract and Their Antimicrobial Activity against Representative Microorganisms. *J. Radiat. Res. Appl. Sci.* **2015**, *8*, 265–275. [CrossRef]
48. Lebaschi, S.; Hekmati, M.; Veisi, H. Green Synthesis of Palladium Nanoparticles Mediated by Black Tea Leaves (*Camellia sinensis*) Extract: Catalytic Activity in the Reduction of 4-Nitrophenol and Suzuki-Miyaura Coupling Reaction under Ligand-Free Conditions. *J. Colloid Interface Sci.* **2017**, *485*, 223–231. [CrossRef] [PubMed]
49. Shende, S.; Ingle, A.P.; Gade, A.; Rai, M. Green Synthesis of Copper Nanoparticles by *Citrus medica* Linn. (Idilimbu) Juice and Its Antimicrobial Activity. *World J. Microbiol. Biotechnol.* **2015**, *31*, 865–873. [CrossRef] [PubMed]
50. Tyagi, A.; Tripathi, K.M.; Singh, N.; Choudhary, S.; Gupta, R.K. Green Synthesis of Carbon Quantum Dots from Lemon Peel Waste: Applications in Sensing and Photocatalysis. *RSC Adv.* **2016**, *6*, 72423–72432. [CrossRef]
51. Isnaeni, I.N.; Indriyati; Dedi; Sumiarsa, D.; Primadona, I. Green Synthesis of Different TiO_2 Nanoparticle Phases Using Mango-Peel Extract. *Mater. Lett.* **2021**, *294*, 129792. [CrossRef]
52. Rojo, C.; Carmona, E.R.; Hernández-Saravia, L.P.; Villacorta, A.; Marcos, R.; Carevic, F.S.; Apablaza, V.H.; Nelson, R. Utilization of Orange Peel Waste for the Green Synthesis of Iron Nanoparticles and Its Application to Stimulate Growth and Biofortification on *Solanum lycopersicum*. *Waste Biomass Valorization* **2024**, *15*, 6343–6356. [CrossRef]
53. Selvaraj, R.; Murugesan, G.; Rangasamy, G.; Bhole, R.; Dave, N.; Pai, S.; Balakrishna, K.; Vinayagam, R.; Varadavenkatesan, T. As (III) Removal Using Superparamagnetic Magnetite Nanoparticles Synthesized Using Ulva Prolifera—Optimization, Isotherm, Kinetic and Equilibrium Studies. *Chemosphere* **2022**, *308*, 136271. [CrossRef] [PubMed]
54. Elizondo-Villarreal, N.; Verástegui-Domínguez, L.; Rodríguez-Batista, R.; Gándara-Martínez, E.; Alcorta-García, A.; Martínez-Delgado, D.; Rodríguez-Castellanos, E.A.; Vázquez-Rodríguez, F.; Gómez-Rodríguez, C. Green Synthesis of Magnetic Nanoparticles of Iron Oxide Using Aqueous Extracts of Lemon Peel Waste and Its Application in Anti-Corrosive Coatings. *Materials* **2022**, *15*, 8328. [CrossRef] [PubMed]
55. Huang, L.; Weng, X.; Chen, Z.; Megharaj, M.; Naidu, R. Green Synthesis of Iron Nanoparticles by Various Tea Extracts: Comparative Study of the Reactivity. *Spectrochim. Acta Part A Mol. Biomol. Spectrosc.* **2014**, *130*, 295–301. [CrossRef] [PubMed]
56. Zayed, M.; Ghazal, H.; Othman, H.A.; Hassabo, A.G. Synthesis of Different Nanometals Using Citrus Sinensis Peel (Orange Peel) Waste Extraction for Valuable Functionalization of Cotton Fabric. *Chem. Pap.* **2022**, *76*, 639–660. [CrossRef]
57. Zakariya, N.A.; Majeed, S.; Jusof, W.H.W. Investigation of Antioxidant and Antibacterial Activity of Iron Oxide Nanoparticles (IONPS) Synthesized from the Aqueous Extract of *Penicillium* spp. . *Sens. Int.* **2022**, *3*, 100164. [CrossRef]
58. Afrouz, M.; Ahmadi-Nouraldinvand, F.; Elias, S.G.; Alebrahim, M.T.; Tseng, T.M.; Zahedian, H. Green Synthesis of Spermine Coated Iron Nanoparticles and Its Effect on Biochemical Properties of Rosmarinus Officinalis. *Sci. Rep.* **2023**, *13*, 775. [CrossRef] [PubMed]
59. Pai, S.; Kini, S.M.; Narasimhan, M.K.; Pugazhendhi, A.; Selvaraj, R. Structural Characterization and Adsorptive Ability of Green Synthesized Fe_3O_4 Nanoparticles to Remove Acid Blue 113 Dye. *Surf. Interfaces* **2021**, *23*, 100947. [CrossRef]
60. Anupong, W.; On-uma, R.; Jutamas, K.; Joshi, D.; Salmen, S.H.; Alahmadi, T.A.; Jhanani, G.K. Cobalt Nanoparticles Synthesizing Potential of Orange Peel Aqueous Extract and Their Antimicrobial and Antioxidant Activity. *Environ. Res.* **2023**, *216*, 114594. [CrossRef] [PubMed]
61. Keerthika Devi, R.; Ganesan, M.; Chen, T.-W.; Chen, S.-M.; Akilarasan, M.; Shaju, A.; Rwei, S.-P.; Yu, J.; Yu, Y.-Y. In-Situ Formation of Niobium Oxide–Niobium Carbide–Reduced Graphene Oxide Ternary Nanocomposite as an Electrochemical Sensor for Sensitive Detection of Anticancer Drug Methotrexate. *J. Colloid Interface Sci.* **2023**, *643*, 600–612. [CrossRef] [PubMed]
62. Suen, N.-T.; Hung, S.-F.; Quan, Q.; Zhang, N.; Xu, Y.-J.; Chen, H.M. Electrocatalysis for the Oxygen Evolution Reaction: Recent Development and Future Perspectives. *Chem. Soc. Rev.* **2017**, *46*, 337–365. [CrossRef] [PubMed]

63. Liu, C.; Ma, H.; Yuan, M.; Yu, Z.; Li, J.; Shi, K.; Liang, Z.; Yang, Y.; Zhu, T.; Sun, G.; et al. (NiFe)S2 Nanoparticles Grown on Graphene as an Efficient Electrocatalyst for Oxygen Evolution Reaction. *Electrochim. Acta* **2018**, *286*, 195–204. [CrossRef]
64. Qi, J.; Zhang, W.; Xiang, R.; Liu, K.; Wang, H.; Chen, M.; Han, Y.; Cao, R. Porous Nickel–Iron Oxide as a Highly Efficient Electrocatalyst for Oxygen Evolution Reaction. *Adv. Sci.* **2015**, *2*, 1500199. [CrossRef] [PubMed]
65. Zhang, Z.; Qin, Y.; Dou, M.; Ji, J.; Wang, F. One-Step Conversion from Ni/Fe Polyphthalocyanine to N-Doped Carbon Supported Ni-Fe Nanoparticles for Highly Efficient Water Splitting. *Nano Energy* **2016**, *30*, 426–433. [CrossRef]
66. Yang, L.; Guo, Z.; Huang, J.; Xi, Y.; Gao, R.; Su, G.; Wang, W.; Cao, L.; Dong, B. Vertical Growth of 2D Amorphous $FePO_4$ Nanosheet on Ni Foam: Outer and Inner Structural Design for Superior Water Splitting. *Adv. Mater.* **2017**, *29*, 1704574. [CrossRef] [PubMed]
67. Wu, G.; Chen, W.; Zheng, X.; He, D.; Luo, Y.; Wang, X.; Yang, J.; Wu, Y.; Yan, W.; Zhuang, Z.; et al. Hierarchical Fe-Doped NiOx Nanotubes Assembled from Ultrathin Nanosheets Containing Trivalent Nickel for Oxygen Evolution Reaction. *Nano Energy* **2017**, *38*, 167–174. [CrossRef]
68. Zou, H.-H.; Yuan, C.-Z.; Zou, H.-Y.; Cheang, T.-Y.; Zhao, S.-J.; Qazi, U.Y.; Zhong, S.-L.; Wang, L.; Xu, A.-W. Bimetallic Phosphide Hollow Nanocubes Derived from a Prussian-Blue-Analog Used as High-Performance Catalysts for the Oxygen Evolution Reaction. *Catal. Sci. Technol.* **2017**, *7*, 1549–1555. [CrossRef]
69. Huang, H.; Yu, C.; Zhao, C.; Han, X.; Yang, J.; Liu, Z.; Li, S.; Zhang, M.; Qiu, J. Iron-Tuned Super Nickel Phosphide Microstructures with High Activity for Electrochemical Overall Water Splitting. *Nano Energy* **2017**, *34*, 472–480. [CrossRef]
70. Liu, J.; Zhu, D.; Ling, T.; Vasileff, A.; Qiao, S.-Z. S-$NiFe_2O_4$ Ultra-Small Nanoparticle Built Nanosheets for Efficient Water Splitting in Alkaline and Neutral PH. *Nano Energy* **2017**, *40*, 264–273. [CrossRef]
71. Yan, K.; Sheng, M.; Sun, X.; Song, C.; Cao, Z.; Sun, Y. Microwave Synthesis of Ultrathin Nickel Hydroxide Nanosheets with Iron Incorporation for Electrocatalytic Water Oxidation. *ACS Appl. Energy Mater.* **2019**, *2*, 1961–1968. [CrossRef]
72. Manso, R.H.; Acharya, P.; Deng, S.; Crane, C.C.; Reinhart, B.; Lee, S.; Tong, X.; Nykypanchuk, D.; Zhu, J.; Zhu, Y.; et al. Controlling the 3-D Morphology of Ni–Fe-Based Nanocatalysts for the Oxygen Evolution Reaction. *Nanoscale* **2019**, *11*, 8170–8184. [CrossRef] [PubMed]
73. Zhao, B.; Zheng, Y.; Ye, F.; Deng, X.; Xu, X.; Liu, M.; Shao, Z. Multifunctional Iron Oxide Nanoflake/Graphene Composites Derived from Mechanochemical Synthesis for Enhanced Lithium Storage and Electrocatalysis. *ACS Appl. Mater. Interfaces* **2015**, *7*, 14446–14455. [CrossRef] [PubMed]
74. Liu, S.; Li, L.; Yang, T.; Wang, E.; Yu, X.; Hou, Y.; Du, Z.; Cao, S.; Chou, K.-C.; Hou, X. Enhanced Overall Water Splitting by Morphology and Electronic Structure Engineering on Pristine Ultrathin Metal-Organic Frameworks. *J. Mater. Sci. Technol.* **2025**, *220*, 92–103. [CrossRef]